Inherent characteristics of ultra-photosensitive Al/Cu–CeO_2/p-Si metal oxide semiconductor diodes

V. Manikandan,[a] R. Marnadu,[b] J. Chandrasekaran,[c] S. Vigneselvan,[d] R. S. Mane,[e] Craig E. Banks[f] and Ali Mirzaei[g]

An ultrahigh photosensitive diode was developed using a Cu-doped CeO_2 thin film through spray pyrolysis processing, which has made a unique contribution in the field of optoelectronic device fabrication process. Phase identification revealed a good arrangement of atoms in the as-prepared nanostructured thin films *via* structural analysis. The formation of wire-shaped nanorods was confirmed. Elemental distribution and their valence states were systematically monitored using X-ray photoelectron spectroscopy analysis, where the presence of Ce^{3+} was evidenced. Good mechanical properties were obtained owing to the Cu-doping in the cerium host matrix, which was investigated by nano-indentation. Bandgap energy fluctuation was the root cause for electrical conductivity. The present work revealed a decrease in the band gap energy upon Cu-doping alters the electrical conductivity. An as-fabricated photodiode demonstrated superior detectability upon Cu-doping. In the depletion region, on account of a high surface-to-volume ratio, the generation of electron–hole pairs increased along with photoresponsivity with increases in the quantum efficiency and current gain.

1. Introduction

Photodetectors easily perceive light or electromagnetic radiation and are widely used in communication systems, environmental monitoring, flame monitoring, military surveillance, chemical/biological analysis and missile tracking.[1,2] According to the thermo-ionic field emission, the reverse leakage currents are produced under reverse bias condition in a Schottky diode. To overcome the leakage of current, metal-oxide-semiconductor diodes can be used. The leakage current influences the detection of UV light.[3] Metal-oxide-semiconductor diodes increase the charge-carrier mobility, while they decrease the charge leakage to ensures the device performance. Here, valence compounds could be endowed with a high degree of ionic bonding and their conduction band became a minimum, whereas valence bands have metal and oxygen 2p orbitals. This increases charge-carrier transport during the interaction of the metal and oxygen in the orbitals. So, the mobility is increased in metal-oxide semiconductors.[4,5] Owing to the insertion of an oxide layer, the dark current of metal-oxide-semiconductor diodes decreases. This means that the ideality factor and barrier height can be reduced upon increasing the photosensitivity of the device.[6]

Metal oxide thin films make it simple to integrate various electronics and also allow encompassing a unique surface morphology, and so are widely used in advanced electronic devices. Traditionally, the doping of different material constructs different structures in the middle of a metal-oxide-semiconductor interface, ensuring the ability of the device.[7] Due to the doping, the surface-to-volume ratio, charge-carrier life time, electrical conduction, and rapid light absorption are improved. The mechanical strength of the thin film was found to be good in terms of the surface morphology, which facilitated better housing for the charge carriers, which is important as optical absorption plays a significant role in optoelectronic devices. Further, the optical properties might be influenced by the mechanical strength, which implies the surface roughness of a material. Smooth surfaces often expediate electron transfer that can be replicated in optical absorption. Also, a slight change in surface roughness changes the light intensity passed to thin films.[8] Weak optical absorption is beneficial for solar cells, organic light-emitting diodes, and LCD panels, but it is detrimental to active optoelectronic systems that require a strong light–matter interaction.[9] Particularly, nanostructured

[a] *Department of Physics, Kongunadu Arts and Science College, Coimbatore – 641 029, India. E-mail: manikandan570@gmail.com*
[b] *PG Department of Physics, G.T.N. Arts College, Dindigul 624 005, India*
[c] *Department of Physics, Sri Ramakrishna Mission Vidyalaya College of Arts and Science, Coimbatore 641 020, India*
[d] *Department of Physics, Government College of Technology, Coimbatore 641 013, India*
[e] *Center for Nanomaterial & Energy Devices, Swami Ramanand Teerth Marathwada University, Dnyanteerth, Vishnupuri, Nanded 431606, India*
[f] *Faculty of Science and Engineering, Manchester Metropolitan University, Chester Street, Manchester M1 5GD, UK*
[g] *Department of Materials Science and Engineering, Shiraz University of Technology, Shiraz, Iran*

thin films have strong light–matter interaction, whereas optical absorption can be increased by two ways: nanostructured thin films and doping. High optical absorption has led to the utmost photoresponsivity of diodes.[10] Wide-bandgap semiconductors have also been shown to be a feasible material for photodetector fabrication due to their high electrical conductivity. Wide-bandgap semiconductors have high intrinsic resistivity because they are deposited under a fixed temperature (500 ıC) and also they possess temperature-dependent resistivity behaviour. The deposition or annealing temperature increases the resistivity of thin films. Ultimately, temperature plays a crucial role in the resistivity of a material.[11] Here, cerium was used as a host material and classified with lanthanide ions, which have attracted much attention owing to the adequate adhesion to solid surfaces and better thermal stability.[12] It has unshielded 5d electrons, where the emission bands induced *via* 5d–4f transitions are highly influenced by doping. Also, the transitions become broad.[13] Cerium invokes redox activity, which ensures electrochemical behaviour.[14] This means that cerium encompasses oxidation and reduction simultaneously.[15] In addition, cerium has double valence states, which enhances the mobility of charge carriers.[16] Surface defects are also involved in cerium materials, *i.e.* oxygen vacancies. Oxygen vacancies increase during Cu-doping. Vigneselvan *et al.* confirmed this feature by doping Cu into a cerium matrix for a humidity sensor.[17] Actually, they found that the resistivity decreased whereas the conductivity increased owing to the oxygen vacancy and carrier concentration. Here, oxygen vacancies play the role of doubly ionized donors. Also, the surface morphology of the thin film surface is an additional factor to raising the conductivity, which is dominated by a doping process, the thickness, concentration of doping and film deposition temperature. The spray pyrolysis technique has vigorously been employed to fabricate thin films of metal oxides and chalcogenides, and offers a number of major advantages, such as homogeneous coating, economical, huge area coverage, and low deposition time.

In this work, Cu was doped into a cerium host matrix through the spray pyrolysis technique. The as-obtained thin films were examined for their structure, morphology, and optical and electrical properties. The pristine cerium oxide (CeO_2) and Cu-doped CeO_2 films were sandwiched in the middle of an Al and *p*-Si layer for increasing a photodetector device performance. The as-fabricated photodetectors were scrutinized for their photosensitivity (P_s), responsivity (R), external quantum efficiency (EQE), specific detectivity (D^*), ideality factor (n), barrier height (f_B) and saturation current (I_0). To the best of our knowledge, the as-obtained Cu-doped CeO_2 thin films endowed ultrahigh photosensitivity, where the diode parameters were amplified *via* Cu-doping. The specific diode parameters were compared with reported works in Table 1. From that table, it can be seen that the Al/Cu–CeO_2/p-Si metal oxide semiconductor diode demonstrated notable results and also ultra-photosensitive (weak signal detection) and superior detectivity.

2. Experimental details

The precursor solution of the Cu–CeO_2 mixture was derived from $CuCl_2{\cdot}2H_2O$ and $CeCl_3{\cdot}7H_2O$ salts. These precursors were prepared according to the stoichiometric composition of x = 0.2, 0.4 M and poured in to dilute ethanol solution. The precursor solution was stirred well until a partially transparent yellow coloured solution was obtained, which was filled in to a spray gun. The precursor solution was sprayed on borosilicate glass substrate. Before deposition, the substrate was rinsed *via* an ultrasonic gator and then dipped in isopropyl alcohol. The substrate was clear and free from dust. The glass substrate was heated to 500 ıC and then the films were coated using the spray. Throughout the process, the deposition temperature was maintained at 500 ıC. Finally, the expected Cu-doped CeO_2 thin films were obtained.

2.1 Al/Cu–CeO_2/p-Si metal oxide diode fabrication

First, the p-type silicon substrate (1 cm × 1 cm) was manipulated for the semiconductor in diode manufacturing. Silicon had a [111] orientation, 279 mm thickness and 60 O resistivity. It also featured monolithic integrability, which refers to the indirect bandgap of silicon. Silicon increases the photodetector responsivity. Usually, a silicon substrate is obtained with organic impurities and the substrates are dipped in a piranha solution for 15–20 min to remove the impurities. Here, pristine cerium oxide and Cu-doped cerium oxide solution were coated

Table 1 Al/Cu–CeO_2/p-Si metal oxide semiconductor diode results compared with reported works

Materials	Photoresponsivity (P_S)	Quantum efficiency (QE) (%)	Detectivity (D^*) (Jones)	Ref.
$In_xGa_{1-x}Sb$/InAs	0.72 A W^{-1}	23.3	2.4×10^9	18
Al/C60/PCPDTBT:PC70BM/PS-TPD-PFCB/PEDOT:PSS/ITO	0.22 mW cm^{-2}	33	5.4×10^{11}	19
Al/a-IGZO/SiO_2/*p*-Si	1.9 × 103 A W^{-1}	—	6.9×10^{11}	20
n-Si (111)/*p*-NiO heterojunction	0.44 mA W^{-1}	20	1.5×10^{10}	21
Pt/PbSe CQDs	0.96 A W^{-1}	78	8.1×10^9	22
Pt-$CH_3NH_3PbBr_3$-Au	2 mA W^{-1}	—	1.4×10^{10}	23
Al/CDC/*p*-Si	47 mA W^{-1}	18.3	—	24
Al/Cu_5FeS_4	1.52 A W^{-1}	—	27.7×10^9	25
Ti/AuWS_2/SiO_2/*p*-Si	0.52 mA W^{-1}	—	4.9×10^9	26
SnS_2/SiO_2/Si	8.8 mA W^{-1}	2.4	2×10^9	27
Al/Cu–CeO_2/p-Si	612.10 mA W^{-1}	237.34	0.5059×10^{12}	Present work

on the surface of the Si substrate. An aluminium (Al) metal contact layered architecture was fabricated for CeO_2/p-Si and Cu–CeO_2/p-Si. Silver paste was applied on both faces of the diode, which eventually facilitated better electrical contact. Finally, the as-fabricated diode was characterized by two modes of operation: forward and reverse bias. Under this bias, the width of the depletion layer was changed and it can be used in different electrical circuits.

2.3 Characterization

Phase identification of the as-prepared thin films was explored *via* X-ray diffraction (XRD, XPERT-PRO). The surface morphology was obtained by field-emission scanning electron microscopy (FESEM, Model FEI quanta 250). A surface-sensitive technique conferred the elemental composition, chemical state and electronic structure of the thin films (AXIS Supra +). The thin films absorbed ultraviolet light and conferred distinct spectra (Model V-770PC). The emission of spontaneous light through optical excitation for probing discrete energy levels was studied by photoluminescence (Model FP8300). A nano-indentation technique was utilized for obtaining the mechanical properties, such as surface roughness, elastic modulus and hardness (TI 700 Ubi; Hysitron). Electrical tests for voltage/current measurements were accomplished on a Keithley electrometer (6517B Electrometer). The fabricated device was scrutinized through dark/photocurrent measurements using a portable solar simulator (Model PEC-L01) (wavelength range: 400–1000 nm).

3. Results and discussion

Fig. 1 presents the XRD spectra of the pristine and Cu-doped CeO_2 thin films according to the different Cu compositions.

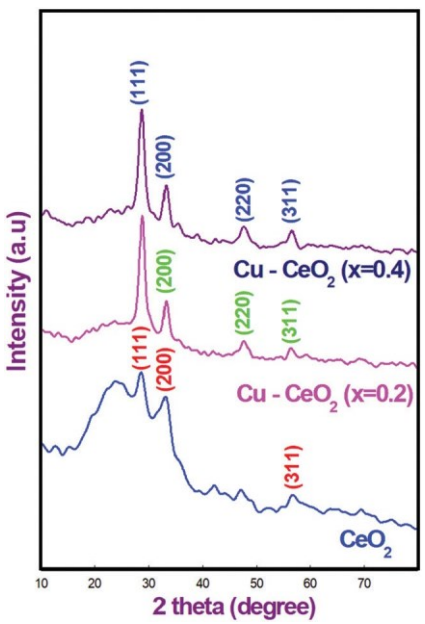

Fig. 1 XRD patterns of the pristine and Cu-doped CeO_2 thin films.

The thin films yielded different orientations of reflection planes, which were not limited to (111), (200), (311) and (220). The orientation of the reflection planes confirmed that the thin films were free from additional reflection planes, namely impurity phases. In this characterization, the most preferential orientation of (111) displayed a distinct peak. An increased (111) intensity peak could be due to the association of Cu into the cerium oxide lattice.[18] The structural parameters listed in Table 1 endowed the crystallite size from 9 to 19 nm with the Cu concentration. Here, the excessive positive charge could be substituted in octahedral or tetrahedral sites, which were compensated through the cation vacancies. For this reason, the smallest crystallite size was observed.[19] The lattice constant increased primarily for low level doping and then decreased for further Cu-doping, which could be facilitated by the ionic radii of the substituted cations. However, the substituted cation size was smaller than the displaced cations, which led to unit cell shrinkage. The movement of cerium atoms between the crystallite and grain boundaries led to a decrease in microstrain in addition to the lattice imperfections.[20] This process can be termed as a recrystallization process.[21] The dislocation density decreased due to the decrease in the number of nucleation sites.[22] The stacking fault values simply overlooked the crystal imperfections.[20] The mentioned crystal imperfection decreased with the Cu substitution. From these structural parameters, the unit cell was shrunken and the lattice imperfections could be compensated *via* Cu deposition on to the CeO_2 thin film Table 2.

Fig. 2(a–c) show the FE-SEM images of the nanorods of the pristine and Cu-doped CeO_2 thin films and their change in size with the Cu concentration. The morphology of the nanorods was confirmed using the length of the nanorods. Also, the size of the nanorods was found to be 3–8 nm, calculated using ImageJ software.[23] As per the view of the surface morphology of the films, the deposits were uniformly coated on the substrate and there were no striking differences, although the pristine cerium film revealed a difference as a result of the Cu incorporation into the cerium host matrix. From Fig. 2(b and c), nanorods were obtained with a high surface area for better conductivity owing to the electron transfer between the grains.[24]

Fig. 3 shows the excellent absorption spectra of the pristine and Cu-doped CeO_2 thin films. From the figure, the absorption edge could existing at different wavelengths, *i.e.* 271, 300, 315 and 466 nm. Two different absorption edges at 271 and 300 nm were noticed in the Cu-doped and pristine CeO_2 thin films. Out of these three films, the Cu-doped CeO_2 thin film with the concentration of $x = 0.4$ showed the maximum absorption edge at 315 nm. Here, the absorption intensity was increased due to the doping. Commonly, the absorption edges of 271 and 300 nm are noticed for doped and undoped CeO_2 thin films at $x = 0.2$. At a higher Cu concentration, the absorption edge of 271 nm was present, but since the absorption edge of 300 nm was shifted to 315 nm, this established the maximum absorption edge. The absorption edge of 271 nm was attributed to the charge transition from O^{2-} to Ce^{3+}. The latter two absorption

Table 2 Physical parameters of the pristine and Cu-doped CeO_2 thin films

Material	Crystallite size (nm)	Lattice constant (Å)	Microstrain (e) ($\times 10^{-3}$ lines^{-2} m^{-4})	Dislocation density (d) ($\times 10^{14}$ lines m^{-4})	Stacking fault (SF) ($\times 10^{-2}$)
CeO_2	09.69	5.385	4.81	2.62	1.71
Cu–CeO_2 ($x = 0.2$)	19.60	5.394	3.04	1.11	1.04
Cu–CeO_2 ($x = 0.4$)	14.84	5.387	3.34	1.23	1.14

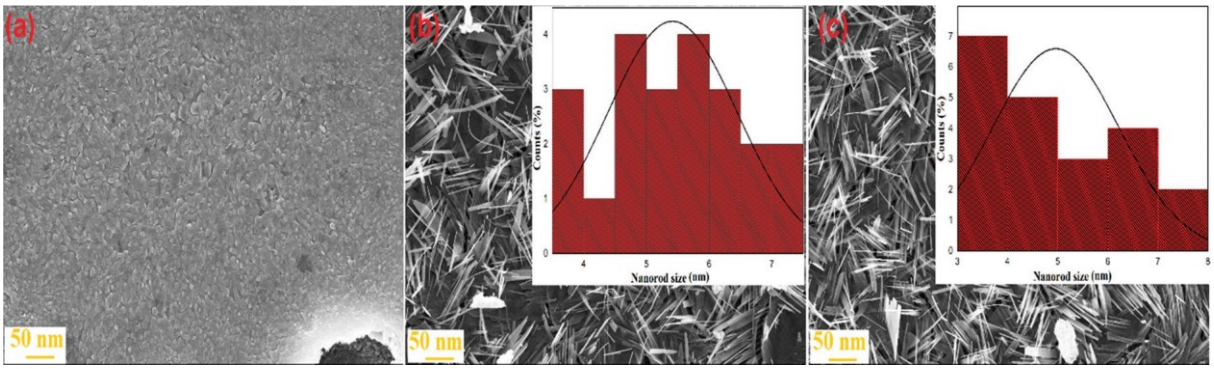

Fig. 2 FE-SEM images of the pristine and Cu-doped CeO_2 thin films.

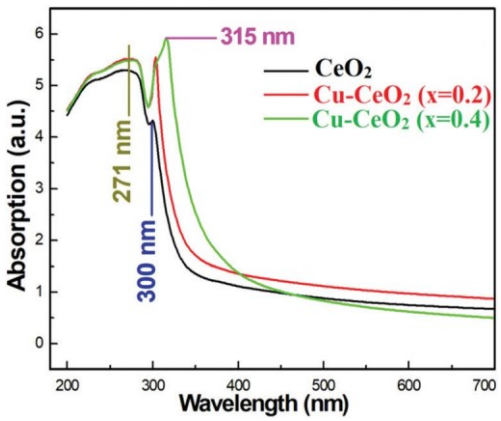

Fig. 3 Absorbance spectra of the pristine and Cu-doped CeO_2 thin films.

edges at 300 and 315 nm were due to the charge transition from O^{2-} to Ce^{4+} and to interband transition.[25] The charge transition affected the crystallinity and optical properties of the thin films. The Cu-doped CeO_2 thin films unveiled strongest absorptions compared to the undoped CeO_2 thin film. The concentration of Ce^{3+} ions depends on the intensity of absorption peak. Here, the Cu-doped CeO_2 thin films exhibited intensity increases that established the formation of Ce^{3+} ions and increased oxygen vacancies owing to a charge compensation mechanism.[26] The absorption spectra analysis concluded that the absorption edge was observed at 270–315 nm, whereas no absorption edge could be found above 315 nm. Also, the absorption edge moved progressively to the longer wavelength side owing to the Cu-doping concentration, which designated a red-shift.[27] However, the absorption edge was shifted to longer wavelength, which indicated a moderate size particle formation.[28]

However, the Cu^{2+} ions entered the site of $Ce^{4+/3+}$, which could form an interfacial phase. However, Cu^{2+} ions could get one hole from Ce^{3+} upon producing one electron as a red-shift. Usually, the obtained red-shift depends on the crystallite size and oxidation state. The Cu-doping increased the crystallite size with a red-shift in the visible region and the oxidation state changed[29] from Ce^{4+} to Ce^{3+}, which might have caused the charge transition between O^{2-} to Ce^{3+} and O^{2-} to Ce^{4+}. The absorption spectra of the pristine and Cu-doped CeO_2 thin films unveiled a similar trend, suggesting the negligible impact of the residual organic components on the red-shift for the thin films. Fig. 4(a–c) present the photon energy *vs.* absorption coefficient of the pristine and Cu-doped CeO_2 thin films, where the band gap energies were calculated from Tauc plots. The pristine CeO_2 thin film secured a band gap energy of 1.93 eV, whereas the Cu-doping reduced the band gap energy values of the CeO_2 thin films. From Fig. 4, the Cu-doped and pristine CeO_2 thin films presented a relatively small energy gap. Due to the small band gap, few electrons could receive sufficient energy at room temperature for entering into the conduction band so as to promote electrical conductivity, whereby approving the semiconductor behaviour. Here, the Cu-doping increased the formation of Ce^{3+} states by facilitating localized energy states, *i.e.* nearer to the conduction band. Hence, the band gap values were increased. Also, the localized energy states could create a path for electrons to enter the conduction band upon increasing the conductivity of the thin films.[30]

Fig. 5 depicts the photoluminescence emission spectra of the pristine and Cu-doped CeO_2 thin films taken from the wavelength of 271 nm. The photoluminescence spectra demonstrated a similar trend, but their intensities were varied according to the Cu-doping. The emission peaks were found at 300–470 nm. These emissions were related to the charge transfer between the

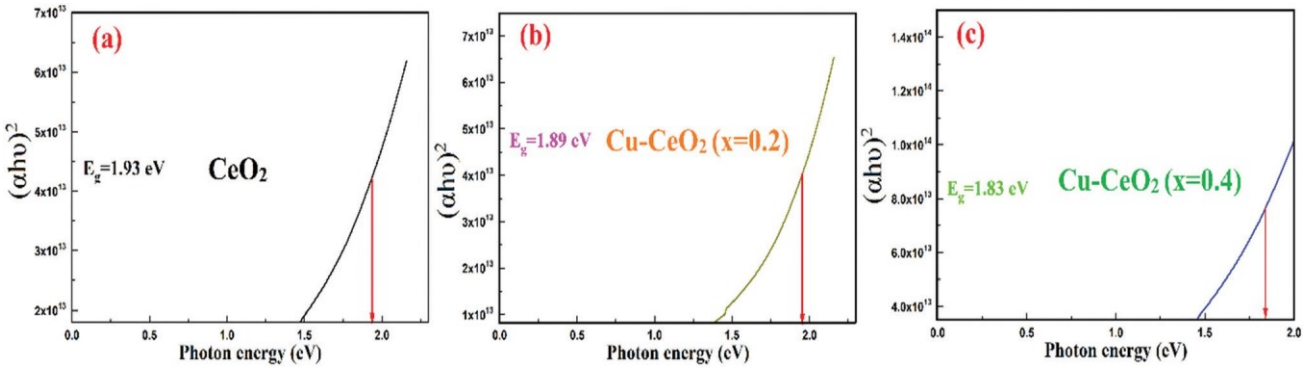

Fig. 4 (a–c) Tauc plots of the pristine and Cu-doped CeO_2 thin films.

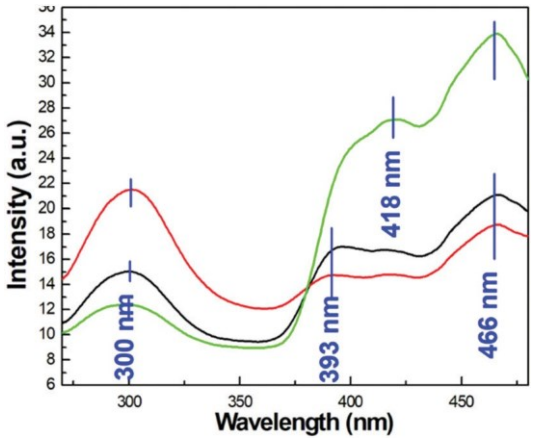

Fig. 5 Photoluminescence spectra of the pristine and Cu-doped cerium oxide thin films.

Ce 4f energy level to the O 2p level, which reflected a localization of the energy level.[31] From the photoluminescence spectra, violet to blue emission was observed at the emitted wavelength and the violet emission was shifted to blue emission at the wavelength of 466 nm. Usually, violet to blue emission is observed from rare earth elements with a distinct peak of 418 nm. The distinct peak correlated with a near-band edge emission.[32] The near-band edge emission was accredited to the recombination of holes and electrons in the valence and conduction bands. Undoped and doped CeO_2 thin films unveiled violet to blue emission around 393 nm. At a higher concentration of Cu, the distinct peak at 418 nm observed from the shift of 393 nm. This shift corresponded to oxygen vacancies and surface defects and these defects facilitated a trapping centre in the band gap, leading to visible emission.[33] Here, we propose a mechanism for the violet to blue emission transition. The electron transition from the donor level was caused *via* interstitial Ce atoms to the valence band. Oxygen defects caused electron transition from the conduction band to the acceptor level, resulting in different band gap energies of the undoped and doped CeO_2 thin films (Fig. 4). This different band gap caused a blue emission shift.[34] The emission peak at 466 nm indicated that the oxygen vacancies and intensity variation was due to Cu-doping, confirming the increase in the oxygen vacancies.[35] All three samples showed common emission peaks close to B2.4 eV, demonstrating the different energy levels of oxygen vacancies in the as-prepared thin films. Therefore, the photoluminescence spectra confirmed the emissions in the visible region were due to the oxygen vacancies. These oxygen vacancies played the role of trapping the excitation energy and this excitation energy was emitted *via* light from the recombination of electrons and holes from the valence band Ce^{3+} trapped holes.[36]

Fig. 6(a–c) denote the XPS spectra of the pristine and Cu-doped CeO_2 thin films. From the spectra, the resultant peaks were for C

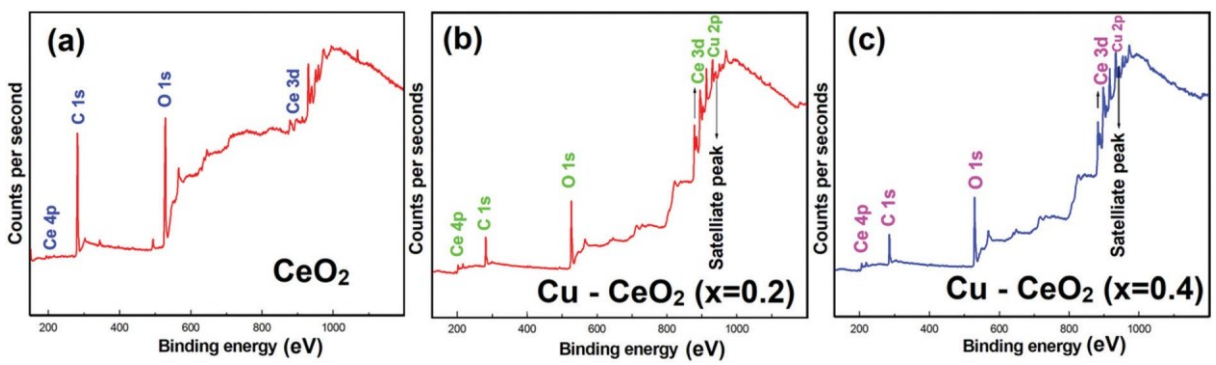

Fig. 6 (a–c) XPS spectra of the pristine and Cu-doped CeO_2 thin films.

(1s), O (1s), Ce (3d), Ce (4p) and Cu (2p). The C 1s peak was positioned at 287–276 eV, which implied the presence of adsorbed impurities. The major peaks of Ce (4p) and Ce (3d) were positioned at 233–199 eV and 924–874 eV. Here, the binding energy of Ce 3d showed doublets, such as Ce $3d_{3/2}$ and Ce $3d_{5/2}$. Those doublet peaks of (916/885) Ce $3d_{3/2}$ and Ce $3d_{5/2}$ (898/882) were attributed to the Ce^{3+} state. This doublet was seen in all samples with spin orbit splitting. The peak area of Ce 3d was wider, describing the characteristics of the Ce^{3+} oxidation state. The O 1s spectrum was positioned at 535–519 eV, which confirmed the oxygen defects or surface oxygen ions.[37] This peak was assigned to C□O bonding.[38] The peak area of O was related to the Cu, while the area for O was reduced due to the doping, which indicated the enrich surface of the Cu-doped cerium material. Additionally, the Cu 2p (933 eV) peak appeared with a weak satellite peak around 940–944 eV, which indicated the Cu^{2+} oxidation state.[39] This satellite peak could be indicative of a small quantity of a secondary phase (CuO). A peak shift was observed from the resultant peaks of O (1s) and Cu (2p), and the remaining peaks were consistent with previous samples. The shift of the O 1s peak was due to the increase in oxygen vacancies. Similarly, the peak shift was detected for Cu (2p), which implied the decrease in binding energy due to the increase in Cu concentration. The binding energy decreased with the increase in the valence electron density.[40] Also, the higher binding energies of O 1s peak supported the formation of Ce^{3+}. On account of the results mentioned here, the material showed the co-existence of Ce^{4+} and Ce^{3+}, and the doping suggested the increase in Ce^{3+} ions.[41,42]

The mechanical properties and surface roughness of the pristine and Cu-doped CeO_2 thin films were examined using nano-indentation tests (Fig. 7(a–f)). The measurements of the root-mean-square (RMS), hardness (H), elastic modulus (E_r) and surface roughness parameters are listed in Table 3. From the figure, the load displacement curves and 3D images deviated, which corresponded to Cu doping. There was a sudden decrease in the hardness and elastic modulus owing to the Cu doping. On the other hand, the progress of the crystallite size changed the hardness and elastic modulus significantly.[43] The oxidation change of cerium could be responsible for this reduction.[44] The mechanical properties of

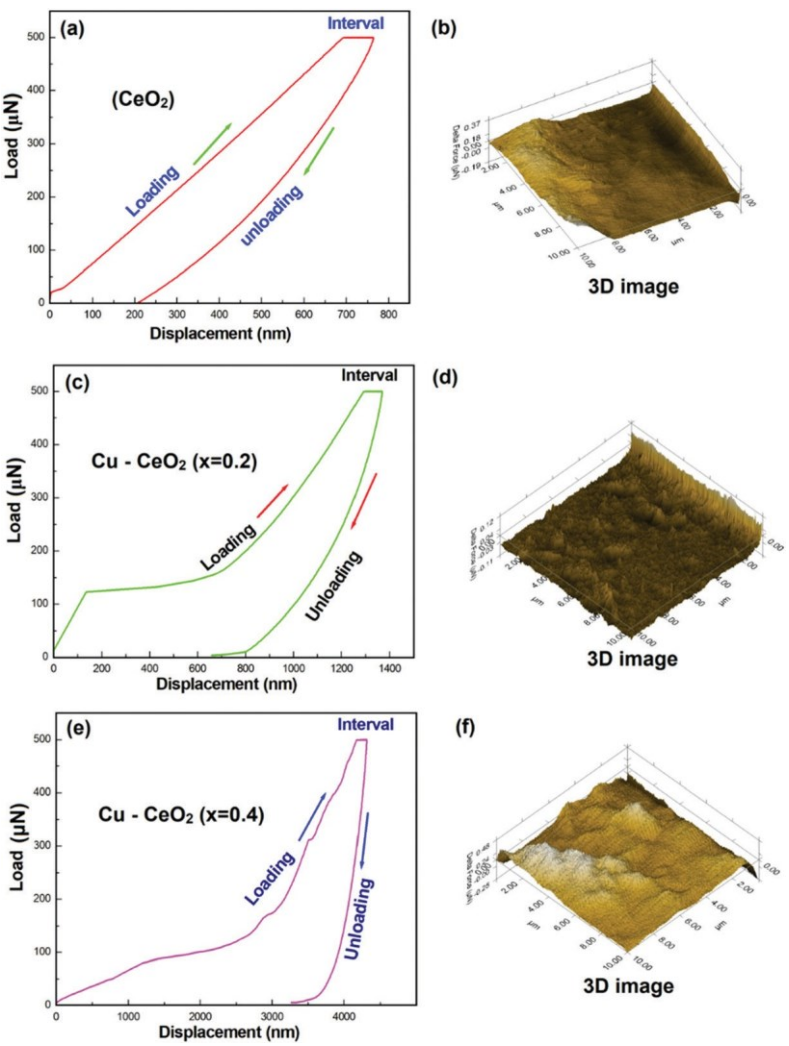

Fig. 7 (a–f) Nano-indentation parameters of the pristine and Cu-doped CeO_2 thin films.

Table 3 Nano-indentation parameters of the pristine and Cu-doped CeO_2 thin films

Materials	Surface roughness (R_a)	RMS (R_q)	Hardness (H) GPa	Elastic modulus (E_r) GPa
CeO_2	71.09	85.25	80.18	489.91
Cu–CeO_2 ($x = 0.2$)	45.53	55.38	15.21	246.67
Cu–CeO_2 ($x = 0.4$)	131.58	150.67	1.22	64.51

the hardness and elastic modulus parameters correlated for the pristine and Cu-doped CeO_2 thin films. From this correlation, the pristine CeO_2 thin film revealed the higher parameters, and the undoped CeO_2 thin film revealed a smaller crystallite size and intense (111) plane. Increased Cu doping provoked a growth in the grain size, which reduced the hardness and elastic modulus.[45] The largest crystallite size of the Cu ($x = 0.4$)-doped CeO_2 thin film led to many dislocations and these dislocations were heaped at the grain boundaries. The movement of dislocations from one grain to neighbouring grains across the grain boundary could be easily achieved and only needed a minimum force, resulting in a decrease in the hardness.[46] From this investigation, the Cu-doped CeO_2 thin film could have sophisticated mechanical properties. From Fig. 7, the loading and unloading curves deviation confirmed the surface smoothness of the thin films. Fig. 7b shows the least deviation compared to the other figures. The figure concludes that the Cu ($x = 0.2$)-doped CeO_2 thin film had a smooth surface. On the other hand, the surface roughness and root-mean-square parameters were changed upon Cu doping. First, both parameters were reduced but then progressed with further doping, as evident from Table 3. Surface roughness is directly related to the electrical conductivity of the thin films. The as-obtained smooth surface of the Cu-doped CeO_2 thin film expedited electron transfer with high electrical conductivity.[47] In addition to this, the root-mean-square parameter showed a similar change in surface roughness. The root-mean-square parameter supported a high value for Cu ($x = 0.4$)-doped CeO_2 thin film with the increase in optical absorption. The progress in optical absorption stimulated the photon carriers. Therefore, the responsivity of the photodiode was escalated by Cu doping.[48]

The forward and reverse bias I–V characteristics of the Al/CeO_2/p-Si and Al/Cu-doped CeO_2/p-Si diodes are shown in Fig. 8. Both in the dark and under light, the photocurrents of the fabricated MOS structure diodes were measured from —3 to +3 V. From Fig. 8, all the MOS diodes showed a drastic variation carriers' long lifetime and the short transit time. From Fig. 8, the value of the photocurrent increased exponentially with increasing the forward voltage. The distance between the sample and illumination head was fixed at 10 cm for all the

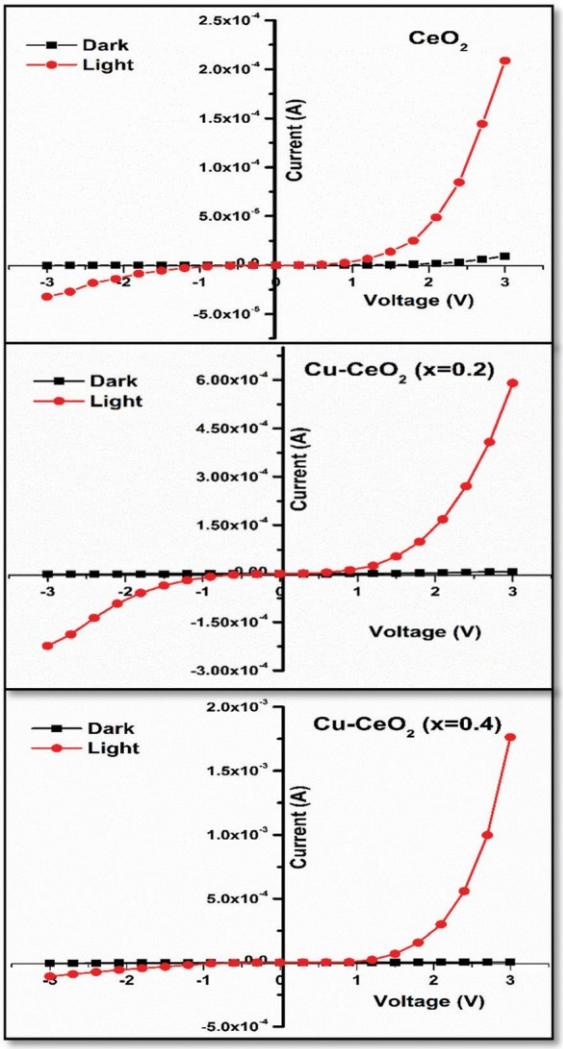

Fig. 8 Forward and reverse bias I–V characteristics of the undoped and doped diodes.

diodes. When compared to pristine CeO_2, the thin oxide layer of Cu-doped CeO_2 between the metal and semiconductor interface showed the larger photocurrent in the order of 10^{-3} Am. The obtained higher photocurrent suggested that the Al/Cu-doped CeO_2/p-Si diode was ultrasensitive under light conditions. The current flow through Al/CeO_2/p-Si and Al/Cu-doped CeO_2/p-Si diodes was investigated using the following equation based on the thermionic emission theory,[49,50]

$$I = AA^*T^2\exp\left(-\frac{q\phi_B}{K_BT}\right)\left[\exp\left(\frac{qV}{nK_BT}-1\right)\right]$$

The reverse saturation current is given by:

$$I_0 = AA^*T^2\exp\left(-\frac{q\phi_B}{K_BT}\right)$$

where I_0 is the reverse saturation current, q is the charge of an electron, V is the bias voltage, n is the ideality factor, F_B is the

effective barrier height, A is the active area of the diode, K_B is the Boltzmann constant, T is the temperature and A^* is the effective Richardson constant. The measured I_0 changed from 2.54 to 4.211 × 10^{-5} A under dark conditions which was 1.23–2.56 × 10^{-4} A under illumination conditions. In a semiconductor diode, the I_0 values are influenced by the diffusion of minority carriers from one region to another. The improvement of I_0 under light-exposed conditions was assigned to the increase in photogenerated carriers. Typically, the diode ideality factor (n) is equal to unity (*i.e.* n = 1), implying the ideal nature of the device, whereas the ideality factor (n) here is more than unity (*i.e.* n = 1), suggesting a non-ideal nature. The diode ideality factor was determined from the intercepts of semi-logarithmic plots of ln J *vs.* voltage (Fig. 9) using the following equation[51,52] as listed in Table 4.

$$n = \frac{q}{k_B T}\frac{dV}{d\ln J} \quad (3)$$

For both the dark and light conditions, the device ideality factor (n) lowered as the Cu concentration increased (Table 4). The presence of Cu ions in the CeO_2 matrix lowered the ideality factor, as shown in Table 4. Moreover, the Al/Cu-doped CeO_2/p-Si with x = 0.4 concentration revealed a better ideality factor (n = 2.29) under light conditions. The conversion efficiency of the interfacial oxide layer (Cu-doped CeO_2), creation of additional charge carriers, suitable absorption of the oxide layer, lesser recombination and large separations of electron–hole pairs could be major reasons for the minimum ideality factor under illumination conditions. Besides, the deviation of the ideality factor from the ideal value was attributed to the presence of a thin oxide layer (SiO_2), image force lowering, density distribution of the interface states or interface traps at the metal–semiconductor interface and barrier inhomogeneity.[52,53] The experimental barrier height of the Al/Cu-doped CeO_2/p-Si diodes was determined using the following equation,[54,55]

$$\Phi_B = \frac{K_B T}{q} \ln \frac{AA^{*}T^2}{I_0} \quad (4)$$

where A^* is the Richardson constant (32 A cm^{-2} K^{-2} for p-type silicon). It can be seen from Table 4 that the estimated barrier height (Φ_B) of the MOS devise was reduced with increasing the Cu concentration up to x = 0.2, both in the dark and light. The decrease in barrier height with increasing the doping concentration was due to the interfacial oxide layer and interface states.[56,57] Also, the higher doping level of x = 0.4 concentration showed an improvement in the Φ_B (Table 3). The higher Φ_B was one of the reasons for the decreasing ideality factor at the higher Cu concentration (x = 0.4). Moreover, the variation of the barrier height in the MOS diodes was attributed to the existence of potential difference across the interfacial oxide layer, the formation of a chemical reaction between the metal–semiconductor interfaces, development of a depletion region and the thickness of the interfacial layer. Also, the structural and morphological changes were inhomogeneous at the MS interface.[57]

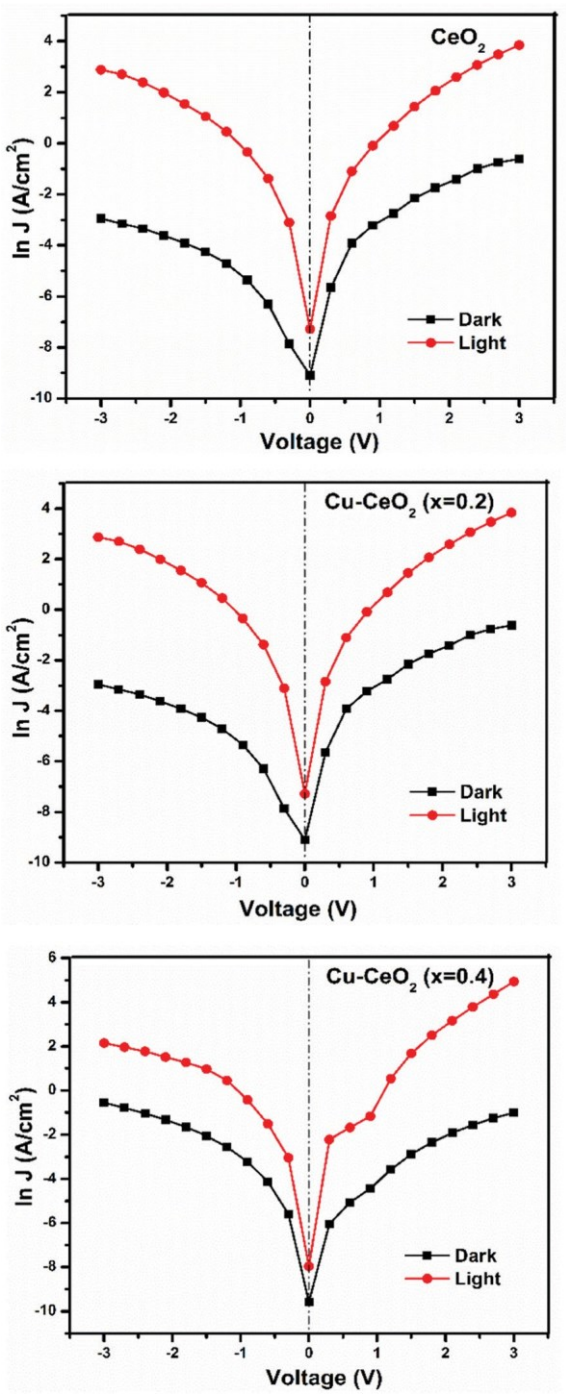

Fig. 9 Semi-logarithmic plots of the undoped and doped diodes.

The photodetector's quality determines the MOS diode's photosensitivity (P_S). The following equation was used to calculate the sensitivity of the fabricated diodes at 3 V.

$$P_S(\%) = \frac{I_{Ph} - I_D}{I_D} \times 100 \quad (5)$$

where I_D is the dark current and I_{Ph} is the photocurrent. The photosensitivity (P_S) of the Al/Cu-doped CeO_2/p-Si diodes increased gradually with the Cu-doping level. The MOS diode

Table 4 MOS structured diodes parameters with different concentrations of Cu

	Ideality factor (n)		Barrier height F_B (eV)		Saturation current I_0 (A)	
Diode	Dark	Light	Dark	Light	Dark	Light
A ($x = 0.0$)	4.99	3.28	0.72	0.67	3.22×10^{-5}	1.97×10^{-4}
B ($x = 0.2$)	3.38	2.59	0.71	0.66	4.11×10^{-5}	2.56×10^{-4}
C ($x = 0.4$)	3.28	2.29	0.73	0.74	2.54×10^{-5}	1.23×10^{-4}

with $x = 0.4$ concentration exhibited a maximum photosensitivity (P_S) of 38492.8%, which was 18 times higher than that of the undoped and 5 times that of the doped diode ($x = 0.2$). The higher photosensitivity indicated the prominence of the oxide layer at the metal–semiconductor contact. The photosensitivity (P_S) of the Al/Cu-doped CeO_2/p-Si diodes increased linearly as the forward voltage was increased from 0 to 3 V (Fig. 9), implying that the addition of Cu ions into the CeO_2 lattice uplifted the photosensitivity of the Al/Cu-doped CeO_2/p-Si diodes. Furthermore, the increased photosensitivity (P_S) of the MOS device was due to optical amplification based on the stimulated emission, which was confirmed by Tanaka.[58] In addition, the presence of light induced e^- and h^+ pairs at the depletion layer, especially near the heterostructure interface of the MOS.[58,59] The ratio of the photocurrent (I_{ph}) to the incident optical power (P) represents the responsivity (R) of the MOS device, which was calculated using the following equation,

$$R = \frac{I_{Ph}}{PA} \quad (6)$$

where I_{Ph} is the photocurrent A is the area of the diode and P is the irradiation of the lamp. From Fig. 10, all the MOS diodes exhibited a similar behaviour of an exponential increment in the responsivity (R) with the applied voltage. Particularly, at 3 V maximum responsivities were recorded of 130.47, 263.64 and 612.10 mA W^{-1} for $x = 0.0$, 0.2, 0.4, respectively. In fact, the lifetime of the photogenerated charge carries and the penetration depth of external light were increased with the responsivity. Comparatively, it was found that a lower wavelength facilitates the light photons penetrating more easily over long distances. The number of e^- and h^+ pairs generation at the depletion region is increased, which improves the overall photoresponsivity of the device. However, the obtained lower responsivity of the undoped diode was due to the short lifetime of the charge carrier due to the higher wavelength.[60] The fabricated MOS device achieved 612.10 mA W^{-1} responsivity, which was much higher than other reported values.[61,62] The quantum efficiency (QE) of the fabricated MOS diodes (in terms of %) was calculated using the obtained responsivity (R) by the following equation,[62]

$$QE = \frac{Rhc}{q\lambda} \quad (7)$$

where R is the responsivity, h is Planck's constant, c is the light velocity, q is the charge of electron and λ is the wavelength. The variations of QE with applied voltage for each diode are shown in Fig. 10. The QE of the Al/Cu-doped CeO_2/p-Si diodes varied from 50.59% to 237.34% with the Cu-doping level. The presence of nanostructured films (Cu-doped CeO_2) with a higher surface-to-volume ratio at the MS interface improved the charge-separation behaviour owing to the increase in the possibility of the oxygen-related h^+-trapping process and the number of surface trap states. Suppose, the energy of external light photons is larger than the band gap of semiconductors (*i.e.* Si = 1.12 eV), whereby the photogenerated electron–hole pairs in the depletion region can be separated by the built-in electric field in the depletion region. Therefore, the photocreated holes (h^+) in the diffusion area away from the depletion edge can also reach the depletion region by the effect of diffusion (Fig. 11). The holes can tunnel through the oxide layer (Cu–CeO_2) and reach the metal (Al), while the e^- move to the back contact due to the relaxation process. Moreover, the depletion region must be as close to the surface as possible in order to reach the optimum responsivity in the ultraviolet region. With the formation of electron–hole pairs at the depletion region of the MOS (tunnelling structure), the MOS photodetector can preserve extreme quantum efficiency. This could be a reason for the increasing QE of the MOS device after doping.[63] Actually, the difference between Eg may be rooted in the acceptor-type (for p-Si) surface states above the valence band (eV) near to the junction. These states or traps are also recombination centres, which can capture and release an electron under illumination or a temperature effect. In other words, the charge in these traps can be easy excited from traps to other traps or to the conduction band when compared to the charge at the valence band. The energy value of these acceptor-type surface states is about 0.10 eV ($=E_{ss} - E_v$) and this value is closer to the difference between Eg for three different metal oxide compositions.

Generally, if the energy of the light photon is greater than that of the band gap of the material, this enhances the photoconduction process. Moreover, the photon energy of visible light ranges from 2 to 2.75 (eV), which was higher than that of our band gap energy. From optical studies, pure CeO_2 films have a bandgap energy of 1.93 eV, which was reduced slightly as 1.89 eV and 1.83 eV after Cu doping ($x = 0.2$ and 0.4). The reduction in the optical band gap will improve the charge-transfer properties of the material. Consequently, the Cu-doped MOS diodes exhibited superior photoresponsivity, detectivity and device performance as compared to undoped diode. The specific detectivity (D^*) is a key parameter to analyse the photodetector performance, which can be defined as the inverse of the noise-equivalent power. The following equation was used to calculate the D^* of the MOS diodes,[64]

$$D^{\omega} = \frac{R}{\delta 2qI_D\flat^{1=2}} \quad (8)$$

The specific D^* of the Al/Cu-doped CeO_2/p-Si diodes was enhanced continuously with the increase in doping (Table 5). The D^* values varied with the forward voltage. The specific detectivity of the MOS device was strongly influenced by doping and the applied voltage. Notably, the MOS device prepared with

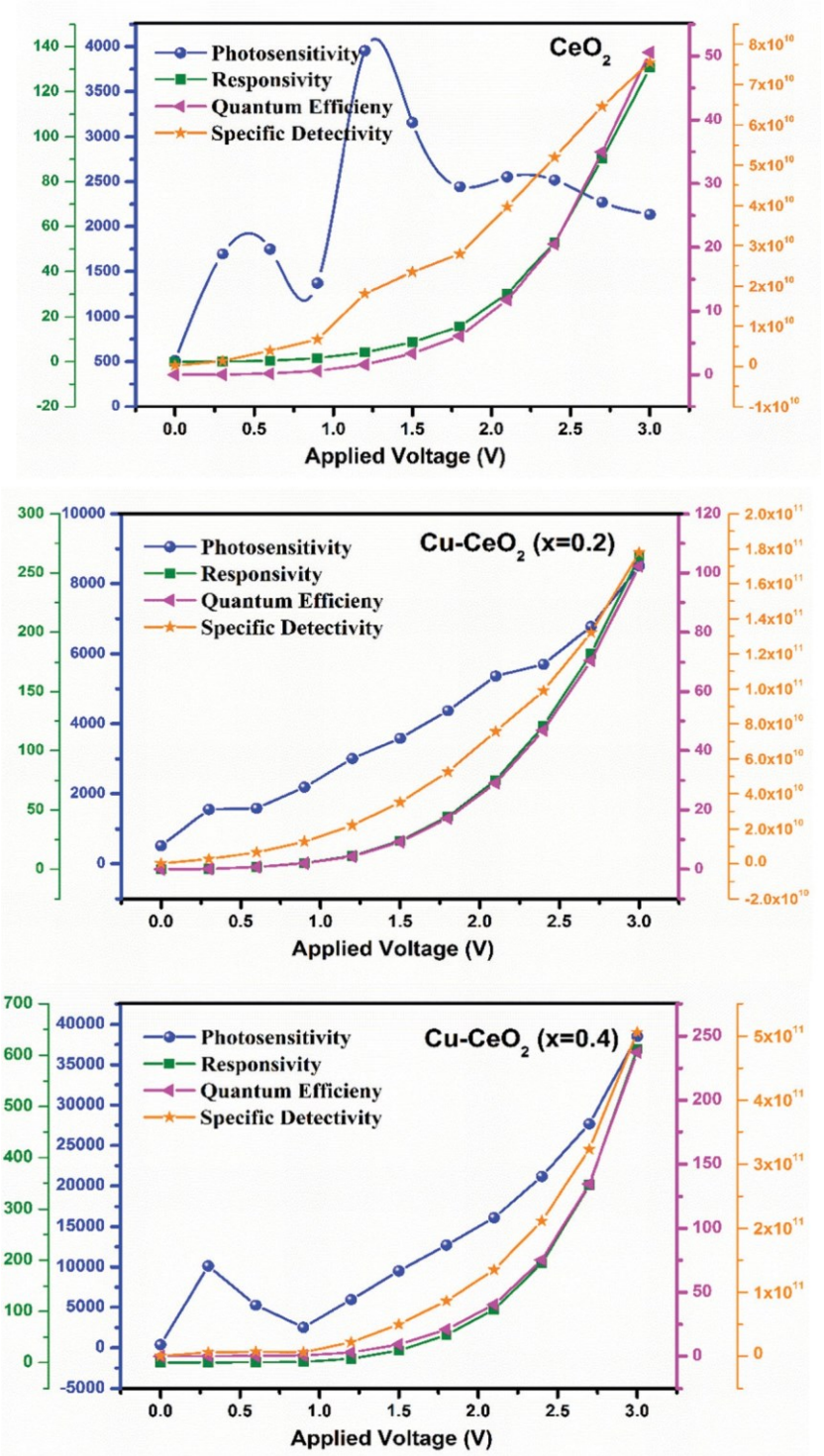

Fig. 10 Variations of the photodetector parameters of the undoped and doped diodes.

$x = 0.4$ concentration revealed a high detectivity of $D^* = 0.5059 \times 10^{12}$ Jones, which is comparatively higher than by Su and Ouyang *et al.*[64–75] The obtained higher detectivity suggests a low noise level of the fabricated MOS diodes. The fabricated MOS diode with superior detectivity (*i.e.* $x = 0.4$) was highly appropriate for detecting a weak signal.

From Fig. 12, the lower wavelength (250–450 nm) showed a higher sensitivity when compared to higher wavelength (700–100 nm). The shorter wavelength has higher energy, which improves the photoresponse of the device. Prominently, the energy of the light photons must be higher than that of the band gap energy of the material. In order to increase the

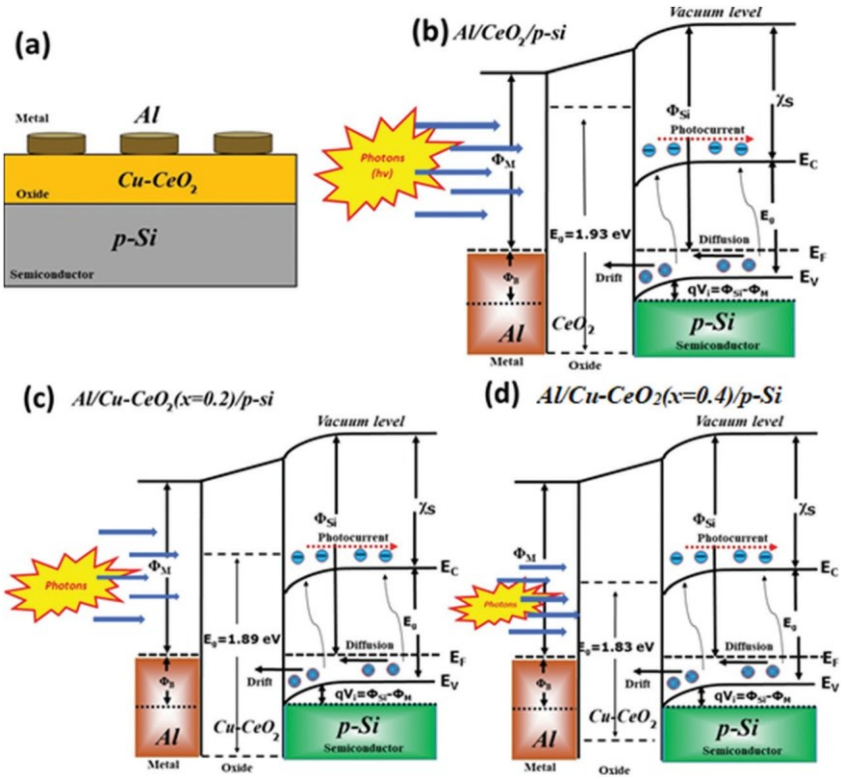

Fig. 11 (a) Schematic diagram of the MOS diode. (b–d) Energy level diagrams of the undoped and doped diodes.

Table 5 Calculated photodetector parameters of the MOS structured diodes at 3 V

Diode	Photosensitivity (%)	Responsivity (mA W^{-1})	Quantum efficiency (%)	Detectivity (Jones)	Current gain
A (x = 0.0)	2137.1	130.47	50.59	7.545×10^{10}	22.37
B (x = 0.2)	8507.2	263.64	102.23	1.778×10^{11}	86.07
C (x = 0.4)	38 492.8	612.10	237.34	0.5059×10^{12}	385.92

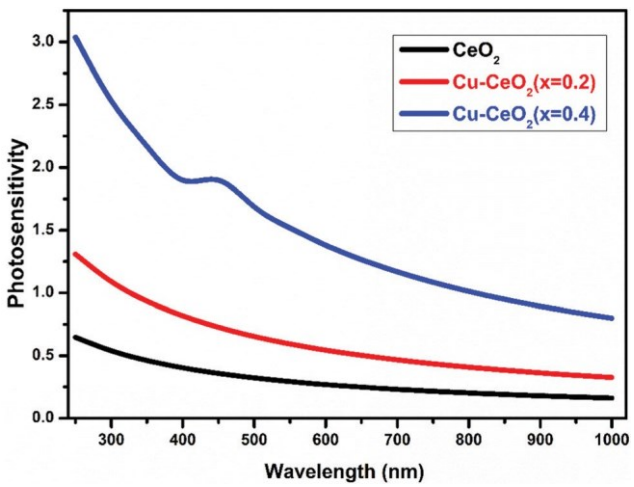

Fig. 12 Photosensitivity of the undoped and doped diodes.

sensitivity at shorter wavelengths, the width of the oxide layer (Cu–CeO_2) might be smaller. Moreover, when the wavelength increases, the energy per photon becomes lesser and each photon can still form a carrier at a lower energy. Thus, the photosensitivity becomes larger at longer wavelengths. However, if the wavelength is too long and the energy of the photon is too low, the photosensitivity will rapidly drop to zero because the necessary condition (*i.e.* $h\nu \geq E_g$) is not satisfied. Here, higher Cu doping showed the maximum responsivity, particularly the wavelength range between 250–450 nm, compared with other doping. From this result, we concluded that the fabricated MOS device was highly sensitive under illumination conditions.

4. Conclusions

Cu-doped CeO_2 nanostructured thin films were prepared by a spray pyrolysis technique and the prepared films were employed as interfacial layers in metal oxide semiconductor diode devices. The thin films were found to have reflection planes and the smallest crystallite sizes. Besides, the diffraction values of Cu-doped CeO_2 were close to the pristine cerium oxide thin films, implying Cu was fully infiltrated in the cerium host matrix. The FE-SEM study confirmed the presence of small-sized

grains and a uniform coating on the films. Eventually, the appearance of the cerium 3+ oxidation state was detected in the Cu-doped CeO_2 nanostructured thin films. A smooth surface was observed in the prepared thin film, which could ensure a better electrical conductivity of the device. The near-band edge emission was observed in the Cu-doped CeO_2 thin films, thus establishing a recombination of holes and electrons in the valence and conduction bands. Also, the band gap energy variation assured a blue-shift in emission and oxygen vacancies. From the diode evaluation, Cu-doped cerium ($x = 0.4$) had significant detectivity of $D^* = 0.5059 \times 10^{12}$ Jones, which suggests a low noise level of the diodes. The fabricated diode was highly suitable to sensing weak signals, which indicated its ultra-photosensitive nature.

Conflicts of interest

There have been no potential conflicts to mention.

Acknowledgements

We are thankful to Assistant Professor, Dr G. Ayyannan, Department of Chemistry, Sri Ramakrishna Mission Vidyalaya College of Arts and Science, for fruitful discussion in this work.

References

1 Y. Kim, S. J. Kim, S. P. Cho, B. H. Hong and D. J. Jang, *Sci. Rep.*, 2015, 5, 1–8.
2 W. Li, X. Zhao, Y. Zhi, X. Zhang, Z. Chen, X. Chu, H. Yang, Z. Wu and W. Tang, *Appl. Opt.*, 2018, 57, 538.
3 T. Oshima, M. Hashikawa, S. Tomizawa, K. Miki, T. Oishi, K. Sasaki and A. Kuramata, *Appl. Phys. Express*, 2018, 11,2–5.
4 N. A. Al-Ahmadi, *Mater. Res. Express*, 2020, 7, 032001.
5 C. W. Shih, A. Chin, C. F. Lu and W. F. Su, *Sci. Rep.*, 2018, 8, 889.
6 T.-Y. Chen and J.-G. Hwu, *ECS J. Solid State Sci. Technol.*, 2014, 3, Q37–Q41.
7 A. Tataroglu, R. Ocaya, A. Dere, O. Dayan, Z. Serbetci, A. G. Al-Sehemi, M. Soylu, A. A. Al-Ghamdi and F. Yakuphanoglu, *J. Electron. Mater.*, 2018, 47, 828–833.
8 A. Vazinishayan, D. R. Lambada, S. Yang, G. Zhang, B. Cheng, Y. T. Woldu, S. Shafique, Y. Wang and N. Anastase, *AIP Adv.*, 2018, 8, 025306.
9 J. Y. Lee, Y. S. Choi, J. H. Kim, M. O. Park and S. Im, *Thin Solid Films*, 2002, 403–404, 553–557.
10 M. A. Squillaci, M. A. Stoeckel and P. Samorì, *Nanoscale*, 2019, 11, 19319–19326.
11 J. Stoever, J. E. Boschker, S. bin Anooz, M. Schmidbauer, P. Petrik, J. Schwarzkopf, M. Albrecht and K. Irmscher, *Appl. Phys. Lett.*, 2020, 116, 182103.
12 Z. Wu, G. Bai, Y. Qu, D. Guo, L. Li, P. Li, J. Hao and W. Tang, *Appl. Phys. Lett.*, 2016, 108, 1–5.
13 G. Bai, M. K. Tsang and J. Hao, *Adv. Funct. Mater.*, 2016, 26, 6330–6350.
14 P. M. Ferreira, J. G. R. C. Gomes and A. Petraglia, *Microelectron. J.*, 2010, 41, 388–394.
15 X. Wang, Y. Teng, Y. Huang, L. Wu and P. Zeng, *J. Nucl. Mater.*, 2014, 451, 147–152.
16 C. H. Lin and C. W. Liu, *Sensors*, 2010, 10, 8797–8826.
17 S. Vigneselvan, V. Manikandan, I. Petrila, A. Vanitha and J. Chandrasekaran, *J. Phys. Chem. Solids*, 2020, 136, 109173.
18 D. H. Wu, Y. Y. Zhang and M. Razeghi, *Appl. Phys. Lett.*, 2018, 112, 111103.
19 X. Gong, M. H. Tong, S. H. Park, M. Liu, A. Jen and A. J. Heeger, *Sensors*, 2010, 10, 6488–6496.
20 B. H. Kang, W. G. Kim, J. Chung, J. H. Lee and H. J. Kim, *ACS Appl. Mater. Interfaces*, 2018, 10, 7223–7230.
21 Y. Zhang, T. Ji, W. Zhang, G. Guan, Q. Ren, K. Xu, X. Huang, R. Zou and J. Hu, *J. Mater. Chem. C*, 2017, 5, 12520–12528.
22 M. Thambidurai, Y. Jang, A. Shapiro, G. Yuan, H. Xiaonan, Y. Xuechao, Q. J. Wang, E. Lifshitz, H. V. Demir and C. Dang, *Opt. Mater. Express*, 2017, 7, 2326.
23 P. A. Shaikh, D. Shi, J. R. D. Retamal, A. D. Sheikh, M. A. Haque, C. F. Kang, J. H. He, O. M. Bakr and T. Wu, *J. Mater.Chem. C*, 2016, 4, 8304–8312.
24 R. Suresh, V. Ponnuswamy, C. Sankar, M. Manickam and R. Mariappan, *Ceram. Int.*, 2016, 42, 12715–12725.
25 S. Sil, A. Dey, J. Datta, M. Das, R. Jana, S. Halder, J. Dhar, D. Sanyal and P. P. Ray, *Mater. Res. Bull.*, 2018, 106, 337–345.
26 C. Lan, Z. Zhou, Z. Zhou, C. Li, L. Shu, L. Shen, D. Li, R. Dong, S. P. Yip and J. C. Ho, *Nano Res.*, 2018, 11, 3371–3384.
27 G. Su, V. G. Hadjiev, P. E. Loya, J. Zhang, S. Lei, S. Maharjan, P. Dong, P. M. Ajayan, J. Lou and H. Peng, *Nano Lett.*, 2015, 15, 506–513.
28 A. Segmüller, I. C. Noyan and V. S. Speriosu, *Prog. Cryst. Growth Charact.*, 1989, 18, 21–66.
29 D. Parimi, V. Sundararajan, O. Sadak, S. Gunasekaran, S. S. Mohideen and A. Sundaramurthy, *ACS Omega*, 2019, 4, 104–113.
30 V. Swaminathan, *Bull. Mater. Sci.*, 1982, 4, 403–442.
31 M. Bedir, A. Tunç and M. Öztas, *Acta Phys. Pol., A*, 2016, 129, 1159–1164.
32 G. Frigerio, C. Mucchino, J. L. Weyher, L. Zanotti and C. Paorici, *J. Cryst. Growth*, 1990, 99, 685–691.
33 M. Srivastava, S. K. Alla, S. S. Meena, N. Gupta, R. K. Mandal and N. K. Prasad, *New J. Chem.*, 2018, 42, 7144–7153.
34 T. Ramesh, K. L. Foo, R. Haarindraprasad, A. J. Sam and M. Solayappan, *Sci. Rep.*, 2019, 9, 1–17.
35 M. Guo, J. Lu, Y. Wu, Y. Wang and M. Luo, *Langmuir*, 2011, 27, 3872–3877.
36 B. M. Reddy, P. Bharali, G. Thrimurthulu, P. Saikia, L. Katta and S. E. Park, *Catal. Lett.*, 2008, 123, 327–333.
37 A. A. Ansari, J. Labis, M. Alam, S. M. Ramay, N. Ahmad and A. Mahmood, *Phase Transitions*, 2016, 89, 261–272.
38 S. Kundu, N. Sutradhar, R. Thangamuthu, B. Subramanian, A. B. Panda and M. Jayachandran, *J. Nanopart. Res.*, 2012, 14, 1040.
39 Z. Liu, B. Guo, L. Hong and H. Jiang, *J. Phys. Chem. Solids*, 2005, 66, 161–167.

40 P. Patsalas, S. Logothetidis, L. Sygellou and S. Kennou, *Phys. Rev. B: Condens. Matter Mater. Phys.*, 2003, 68, 1–13.

41 C. Sun, H. Li, H. Zhang, Z. Wang and L. Chen, *Nanotechnology*, 2005, 16, 1454–1463.

42 T. Monteiro, A. J. Neves, M. C. Carmo, M. J. Soares, M. Peres, E. Alves, E. Rita and U. Wahl, *Superlattices Microstruct.*, 2006, 39, 202–210.

43 S. Sambasivam, D. P. Joseph, S. A. Naidu, K. N. Hui, K. S. Hui and B. C. Choi, *J. Adv. Ceram.*, 2015, 4, 300–306.

44 H. Chen, J. Ding, W. Guo, G. Chen and S. Ma, *RSC Adv.*, 2013, 3, 12327–12333.

45 J. Saranya, K. S. Ranjith, P. Saravanan, D. Mangalaraj and R. T. Rajendra Kumar, *Mater. Sci. Semicond. Process.*, 2014, 26, 218–224.

46 B. Choudhury and A. Choudhury, *Curr. Appl. Phys.*, 2013, 13, 217–223.

47 A. Aranda, E. Aylón, B. Solsona, R. Murillo, A. M. Mastral, D. R. Sellick, S. Agouram, T. García and S. H. Taylor, *Chem. Commun.*, 2012, 48, 4704–4706.

48 D. A. C. Brownson, A. Garcia-Miranda Ferrari, S. Ghosh, M. Kamruddin, J. Iniesta and C. E. Banks, *Nanoscale Adv.*, 2020, 2, 5319–5328.

49 F. A. Al-Agel, E. Al-Arfaj, A. A. Al-Ghamdi, B. D. Stein, Y. Losovyj, L. M. Bronstein, F. S. Shokr and W. E. Mahmoud, *Ceram. Int.*, 2015, 41, 1115–1119.

50 A. Singhania, *Ind. Eng. Chem. Res.*, 2017, 56, 13594–13601.

51 A. Arumugam, C. Karthikeyan, A. S. Haja Hameed, K. Gopinath, S. Gowri and V. Karthika, *Mater. Sci. Eng. Carbon*, 2015, 49, 408–415.

52 T. K. Pathak, E. Coetsee-Hugo, H. C. Swart, C. W. Swart and R. E. Kroon, *Mater. Sci. Eng., B*, 2020, 261, 114780.

53 A. Karthik, S. R. Srither, N. R. Dhineshbabu, N. Lenin, S. Arunmetha, P. Manivasakan and V. Rajendran, *Mater. Charact.*, 2019, 158, 109964.

54 A. Karthik, S. Arunmetha, S. R. Srither, P. Manivasakan and V. Rajendran, *Surf. Coat. Technol.*, 2016, 292, 110–120.

55 H. K. E. Latha, A. Udayakumar and V. Siddeswara Prasad, *Mater. Res. Express*, 2014, 1, 0–12.

56 H. N. Shah, V. Chawla, R. Jayaganthan and D. Kaur, *Bull. Mater. Sci.*, 2010, 33, 103–110.

57 G. Qi, Z. Wu and H. Wang, *J. Mater. Chem. C*, 2013, 1, 7102–7110.

58 M. Yıldırım and A. Kocyigit, *J. Alloys Compd.*, 2018, 768, 1064–1075.

59 S. A. Yeriskin, M. Balbası and İ. Orak, *J. Mater. Sci.: Mater. Electron.*, 2017, 28, 14040–14048.

60 Ş. Altındal, Ö. Sevgili and Y. Azizian-Kalandaragh, *J. Mater. Sci.: Mater. Electron.*, 2019, 30, 9273–9280.

61 O. Çiçek, S. O. Tan, H. Tecimer and -S. Altındal, *J. Electron. Mater.*, 2018, 47, 7134–7142.

62 Y. Badali, Y. Azizian-Kalandaragh, İ. Uslu and Ş. Altindal, *J. Mater. Sci.: Mater. Electron.*, 2020, 31, 8033–8042.

63 M. Özer, D. E. Yildiz, Ş. Altindal and M. M. Bülbül, *Solid-State Electron.*, 2007, 51, 941–949.

64 N. Balaram, M. S. P. Reddy, V. R. Reddy and C. Park, *Thin Solid Films*, 2016, 619, 231–238.

65 V. R. Reddy, *Thin Solid Films*, 2014, 556, 300–306.

66 R. Marnadu, J. Chandrasekaran, M. Raja, M. Balaji, S. Maruthamuthu and P. Balraju, *Superlattices Microstruct.*, 2018, 119, 134–149.

67 M. K. Hudait and S. B. Krupanidhi, *Phys. B*, 2001, 307, 125–137.

68 H. Tanaka, T. Kawazoe and M. Ohtsu, *Appl. Phys. B: Lasers Opt.*, 2012, 108, 51–56.

69 N. K. Hassan, M. R. Hashim and N. K. Allam, *Sens. Actuators, A*, 2013, 192, 124–129.

70 B. E. B. Al-Jumaili, Z. A. Talib, A. Ramizy, N. M. Ahmed, L. Y. Josephine, S. B. Paiman, I. B. Muhd and S. A. Abdulateef, *J. Nanomater.*, 2016, 1, 1890364.

71 X. Gong, M. H. Tong, S. H. Park, M. Liu, A. Jen and A. J. Heeger, *Sensors*, 2010, 10, 6488–6496.

72 R. Suresh, V. Ponnuswamy, C. Sankar, M. Manickam and R. Mariappan, *Ceram. Int.*, 2016, 42, 12715–12725.

73 R. Marnadu, J. Chandrasekaran, S. Maruthamuthu, V. Balasubramani, P. Vivek and R. Suresh, *Appl. Surf. Sci.*, 2019, 480, 308–322.

74 G. Su, V. G. Hadjiev, P. E. Loya, J. Zhang, S. Lei, S. Maharjan, P. Dong, P. M. Ajayan, J. Lou and H. Peng, *Nano Lett.*, 2015, 15, 506–513.

75 B. Ouyang, K. Zhang and Y. Yang, *Adv. Mater. Technol.*, 2017, 2, 1700208.